Hybrid lattice Boltzmann method for multiphase flows

Thomas Gregorczyk, Song Zhao, Pierre Boivin

Hybrid Lattice-Boltzmann method for multiphase flows

Thomas Gregorczyk,* Song Zhao, and Pierre Boivin
Aix Marseille Univ, CNRS, Centrale Med, M2P2, Marseille, France
(Dated: November 3, 2025)

This article presents a new hybrid Lattice-Boltzmann method for simulating multiphase. Mean mass and momentum are solved using a Lattice-Boltzmann method, while an order parameter, indicating whether the fluid is gaseous or liquid, is solved by a classical finite volume scheme.

The Lattice-Boltzmann scheme is adapted from existing methods using a new equilibrium formulation, as well as new macroscopic reconstructions. The consistency of the resulting scheme is confirmed analytically. Validations are then presented for canonical academic cases, as well as 2D liquid jet simulations yielding different breakup covering dripping, sinuous and atomization regimes.

I. INTRODUCTION

Spray nozzles and atomizing jets can be found in a wide variety of applications, ranging from propulsion to perfumery or painting. These applications share the need for a liquid to be dispersed in a fine and rather uniform spray of small droplets, maximizing the interfacial area.

The numerical modeling of such processes presents several challenges. First, the change in fluid properties across interfaces is very large: density ratios on the order of 1000, viscosity changes. The density ratio, in particular, discards most classical numerical methods, which lack robustness in high gradients. Second, the liquid-gas interface has a thickness close to the molecule diameter. Reaching such a spatial discretization, in any of the aforementioned problems, remains unthinkable today: the interface needs to be either smeared numerically – as in multi-fluid [1, 2] or second-gradient methods [3] – or considered as a discontinuity following a tailored equation as in level-set methods [4, 5] and volume-of-fluids methods [6–8]. The literature teems with numerical models to deal with these difficulties, and recent studies now present astounding agreement between experimental data and numerical simulations [9–12]. The proposed methods, while rapidly improving, share the need for a rather intense computational effort which may be prohibitive for the optimization of a practical injector device using current computer architectures.

* Corresponding author: thomas.gregorczyk@centrale-med.fr

In the quest of significantly reducing the cost of numerical simulations of fluid flows, Lattice-Boltzmann methods [13] are being rapidly developed. Being more recent than Navier-Stokes solvers, the method is often not quite as mature for multi-physics problems, but are competitive computationally in most tackled unsteady problems [14]. LBM is also identified as a prime candidate for future quantum computers [15, 16], due to its simpler structure.

LBM is rapidly catching up Navier-Stokes in an ever wider variety of physical problems: aerodynamic [17–19], aeroacoustic [20, 21], compressible [22–24] and reactive flows [25, 26]. LBM solvers have also been tackling multiphase flows for years. As for its Navier-Stokes counterpart, numerical stability is a critical aspect. The intent of this work is to provide new ideas for modeling multiphase flows within the Lattice-Boltzmann framework.

A variety of Lattice-Boltzmann schemes for multiphase flows have been developed over the years [27] and are based on a diffuse interface: color-gradient [28, 29], Shan-Chen (SC) [30], He-Chen-Zhang (HCZ) [31], free-energy [32], phase-field [33] among others. Some of these methods are very similar, for example Lafarge et al. [34] showed that color-gradient and phase-field methods were very close through an appropriate change of variable. Others, like the SC or the free-energy are different and require a non-ideal equation of state to compensate the lack of phase-tracking equation.

In this work we have chosen the phase-field framework [35] for two main reasons. First, it was recently proved very promising for high-density and high-Reynolds flows [33, 36, 37], as encountered in jet atomization. Second, this model has similarities with phase-model Navier-Stokes solvers, which makes it easier to benefit from the Navier-Stokes solvers experience.

The system of equations that we will be solving is composed of two equations for the physical characteristics of the fluids (namely hydrodynamic pressure and momentum) and one to track the interface. This last equation can be solved either via a double-distribution function (DDF) approach which means that we use one LBM distribution for the two NS-like equations and another one for the "phase equation", either via a hybrid approach in which this phase equation is solved using a non-LBM scheme, for example using finite differences. We will use this last option which has barely been studied in the literature and might bring some useful research ideas.

We will start by presenting our numerical method in section II. First we will show our target system of equations in subsection II A then we will present our Lattice-Boltzmann scheme in subsection II B. Finally we will precise our finite difference scheme for the Allen-Cahn equation in subsection II C. Then in section III we will apply this solver on a Poiseuille flow in subsection III A. We will also study the

Laplace (III B) and oscillating droplet (III C) test cases to see that we can correctly recover surface. Subsection III D tackles the Rayleigh-Taylor instability. Our approach to the Allen-Cahn equation is simple and uses its non-conservative formulation. This is a first step that was found to be enough to get correct results as we will see in the rest of this article but which might need improvements in future works like those recently published in [38, 39]. Subsection III E deals with several jet computations at very different regimes.

II. DESCRIPTION OF THE NUMERICAL SCHEME

A. Target equations

The considered governing equations read

$$\begin{cases} \dfrac{\partial \rho u_\alpha}{\partial t} + \dfrac{\partial \left(\rho u_\alpha u_\beta + \mathcal{P}_{\alpha\beta} - \mathcal{T}_{\alpha\beta}\right)}{\partial x_\beta} = \rho \mathcal{F}_\alpha & (1) \\ \dfrac{\partial p}{\partial t} + \rho c^2 \dfrac{\partial u_\alpha}{\partial x_\alpha} = 0 & (2) \\ \dfrac{\partial \phi}{\partial t} + u_\alpha \dfrac{\partial \phi}{\partial x_\alpha} = M \left(\dfrac{\partial^2 \phi}{\partial x_\alpha^2} + \dfrac{1}{W} \dfrac{\partial \left(\phi^2 - 1\right) n_\alpha}{\partial x_\alpha} \right) & (3) \end{cases}$$

with ρ the density, u_α the velocity of the fluid in the direction α, $\mathcal{P}_{\alpha\beta}$ the pressure tensor defined in (5), $\mathcal{T}_{\alpha\beta}$ the viscous stress tensor defined in (6), $\rho\mathcal{F}_\alpha$ forcing terms in the momentum equation, p the hydrodynamic pressure, c the speed of the acoustic waves, ϕ the order parameter, M the mobility factor, W the width of the interface, and n_α the normal to the interface.

The unknowns of the governing equations are hydrodynamic pressure p, momentum ρu_α, and the order parameter ϕ. The system is closed with the following Equation of State (EoS):

$$\rho = \rho_1 \frac{1+\phi}{2} + \rho_2 \frac{1-\phi}{2} \tag{4}$$

with $\rho_{1,2}$ the densities of the fluid 1 and 2. This implies that the system lies in the framework of the incompressible Navier-Stokes equations. Instead of solving an elliptic Poisson equation for the hydrodynamic pressure, we follow the artificially compressible approach (2) [40–42]. In practice, we reduce the physical sound speed to a velocity c,

and we ensure that the fluid velocity is much smaller than that, i.e. $u \ll c$, at any time to justify the incompressible assumption.

The surface tension is embedded in the tensor $\mathcal{P}_{\alpha\beta}$ appearing in the momentum equation (1) which reads

$$\mathcal{P}_{\alpha\beta} \equiv p\delta_{\alpha\beta} + \underbrace{\frac{\sigma}{2|\nabla\phi|}\left(\frac{\partial\phi}{\partial x_\alpha}\frac{\partial\phi}{\partial x_\beta} - |\nabla\phi|^2\delta_{\alpha\beta}\right)}_{\text{Surface tension contribution}} \tag{5}$$

where σ is the surface tension coefficient. This is based on the theory developed by Korteweg [43] who proposed that surface tension contributions to the pressure tensor could be expressed as combinations of gradients of density. Other numerical models also exist and can be found in [44].

The expression of the viscous stress tensor is given by:

$$\mathcal{T}_{\alpha\beta} = \mu\left(\frac{\partial u_\alpha}{\partial x_\beta} + \frac{\partial u_\beta}{\partial x_\alpha} - \frac{2}{D}\frac{\partial u_\gamma}{\partial x_\gamma}\delta_{\alpha\beta}\right) \tag{6}$$

with μ the dynamic viscosity and D the number of dimensions.

We suppose that the two phases are immiscible but due to the diffuse interface model [45, 46] that we use, there will always be some mixing at the interface. We make the hypothesis that pressure and velocity equilibration between the phases are infinitely fast [47]. This enables us to consider only one velocity and one pressure. We will not be considering thermal effects hence the absence of an energy equation.

B. Lattice-Boltzmann method for pressure and momentum equations

The momentum (1) and hydrodynamic pressure transports (2) are resolved by a Lattice-Boltzmann method. The pressure-based hybrid recursive regularized pressure-based (HRR-p) strategy [48] is adopted here, and adapted to two-phase flows. The equilibrium distribution functions, as well as the forcing terms, are modified with the consideration of potential high density/viscous ratios. The surface tension effects are also considered by an additional term in the collision.

Same as in the HRR-p LBM, during each time step, the classical collision and the

streaming steps will be performed

$$\text{Collision}: \quad f_i^{col} = f_i^{eq} + \left(1 - \frac{\Delta t}{\overline{\tau}}\right) f_i^{neq} + \frac{\Delta t}{2} F_i + \frac{\Delta t}{2} S_i + \Omega_i^{st} \tag{7}$$

$$\text{Streaming}: \quad f_i^{*}\left(x, t + \Delta t\right) = f_i^{col}\left(x - c_i \Delta t, t\right) \tag{8}$$

where f_i^{eq} is the equilibrium distribution, $\overline{\tau}$ the relaxation time, f_i^{neq} the off-equilibrium distribution, F_i the forcing terms corresponding to external forces, which can be expressed by the Guo forcing [49] for instance, S_i the correction terms defined in (17) contributing to achieving a correct viscous tensor, and Ω_i^{st} the term accounting for surface tension defined in (14). Each of these terms will be detailed and explained hereafter.

1. Equilibrium distributions

The equilibrium distributions are modified on the third-order Hermite polynomial coefficients such as to read

$$\Pi_{\alpha\beta\gamma}^{eq} \equiv \sum_i c_{i\alpha} c_{i\beta} c_{i\gamma} f_i^{eq} = \rho u_\alpha u_\beta u_\gamma + \rho_0 c_s^2 \left(u_\alpha \delta_{\beta\gamma} + u_\beta \delta_{\alpha\gamma} + u_\gamma \delta_{\alpha\beta}\right) \tag{9}$$

instead of

$$\Pi_{\alpha\beta\gamma}^{eq,\mathrm{HRR-p}} = \rho u_\alpha u_\beta u_\gamma + \rho c_s^2 \left(u_\alpha \delta_{\beta\gamma} + u_\beta \delta_{\alpha\gamma} + u_\gamma \delta_{\alpha\beta}\right) \tag{10}$$

in the pressure-based compressible LBM. ρ_0 in the above expression is an arbitrary constant reference density, which could be adapted according to different density or viscosity ratios. The motivation for this adjustment is that this will lead to the following relationship between the relaxation time and the fluid viscosity:

$$\tau = \frac{\rho \nu}{\rho_0 c_s^2} = \frac{\mu}{\rho_0 c_s^2} \tag{11}$$

instead of the usual classical one $\tau^{\mathrm{HRR-p}} = \nu / c_s^2$. Note that $\bar{\tau}$ used in the collision (7) is defined as $\bar{\tau} = \frac{\Delta t}{2} + \tau$. In our experience, this modified equilibrium gives better results for test cases where the density or viscosity differences between phases are important, where the original equilibrium led to discontinuities of velocity at the interface as reported previously by several authors [34, 50, 51]. c_s is the lattice speed

of sound, it reads:

$$c_s = \frac{\Delta x}{\sqrt{3}\Delta t} \tag{12}$$

In the end, the full formalism of the equilibrium distribution reads

$$\begin{aligned} f_i^{eq} = \omega_i \Bigg(& \frac{p}{c_s^2} + \rho u_\alpha \frac{\mathcal{H}_\alpha}{c_s^2} + \rho u_\alpha u_\beta \frac{\mathcal{H}_{\alpha\beta}}{2c_s^4} + \\ & \left\{ \rho u_\alpha u_\beta u_\gamma + c_s^2 \left(\rho_0 - \rho\right) \left[u_\alpha \delta_{\beta\gamma} + u_\beta \delta_{\alpha\gamma} + u_\gamma \delta_{\alpha\beta} \right] \right\} \frac{\mathcal{H}_{\alpha\beta\gamma}}{6c_s^6} \Bigg) \end{aligned} \tag{13}$$

where ω_i are the weights associated with the lattice and $\mathcal{H}$ are the Hermite polynomials at the corresponding order and lattice [52, 53].

2. Surface tension terms

In order to cooperate with the surface tension in the momentum balance, the following term is added to the collision operator

$$\Omega_i^{st} = \omega_i \mathcal{P}'_{\alpha\beta} \frac{\mathcal{H}_{\alpha\beta}}{2\overline{\tau} c_s^4} \tag{14}$$

with

$$\mathcal{P}'_{\alpha\beta} \equiv \frac{\sigma}{2\left|\nabla\phi\right|} \left(\partial_\alpha \phi \partial_\beta \phi - \delta_{\alpha\beta} \left|\nabla\phi\right|^2 \right) \tag{15}$$

as the surface tension tensor. In practice, the derivatives in the above equation are evaluated by the following isotropic operator [37, 54–57]

$$\frac{1}{c_s^2 \Delta t} \sum_i^N \omega_i c_{\alpha,i} \phi \left(x_\alpha + c_{\alpha,i} \Delta t \right) = \partial_\alpha \phi + \mathcal{O}\left(\Delta x^2\right) \tag{16}$$

where $c_{\alpha,i}$ represents the lattice velocity i along the direction α and N is the number of discrete velocities. Note that the introduced operator use the same neighbors as the Lattice-Boltzmann scheme, translating to a straight-forward numerical implementation.

3. Off-equilibrium distribution & correction terms

A recursive regularized collision operator [58–60] is adopted for non-equilibrium distribution reconstructions because it showed significant stability improvements [61, 62] over the BGK collision operator (for Bhatnagar-Gross-Krook) [63].

Due to the modifications in the equilibrium distributions (13), new correction terms need to be applied to achieve the correct viscous tensor in Eq. (6), their second-order raw moment reads:

$$\Pi^{\mathcal{F}}_{\alpha\beta} = \rho\mathcal{F}_\alpha u_\beta + \rho\mathcal{F}_\beta u_\alpha + \frac{\partial p}{\partial t}\delta_{\alpha\beta} + \rho_0 c_s^2 \left(1 + \frac{2}{D}\right) \frac{\partial u_\gamma}{\partial x_\gamma}\delta_{\alpha\beta} - \frac{\partial p}{\partial x_\alpha}u_\beta - \frac{\partial p}{\partial x_\beta}u_\alpha - \frac{\partial D^{eq}_{\alpha\beta\gamma}}{\partial x_\gamma} \tag{17}$$

The full Chapman-Enskog analysis of this LBM scheme and the value of $D^{eq}_{\alpha\beta\gamma}$ can be found in appendix B.

4. Flow fields transport

The velocity field is reconstructed from the distribution classically as

$$u_\alpha\left(t + \Delta t\right) = \frac{1}{\rho\left(t + \Delta t\right)} \sum_i^N c_{i,\alpha} f_i^* + \frac{\Delta t}{2}\mathcal{F}_\alpha \tag{18}$$

with the density field directly from the EoS in Eq. (4) using the order parameter ϕ.

The hydrodynamic pressure field is transported using the same population. In practice, we evaluate the velocity divergence by

$$\nabla \cdot u \doteq \sum_i^N \left(\frac{f_i^{col}}{\rho} - \left(\frac{f_i^{col}}{\rho}\right)^* \right) \tag{19}$$

with $\left(f_i^{col}/\rho\right)^*$ the quantity f_i^{col}/ρ streamed. Indeed, the Taylor expansion of this operator gives

$$\sum_i \left(\frac{f_i^{col}}{\rho} - \left(\frac{f_i^{col}}{\rho} \right)^* \right) = \sum_i \left(\frac{f_i^{col}}{\rho}(x,t) - \frac{f_i^{col}}{\rho}(x - c_i \Delta t, t) \right) \tag{20}$$
$$= \Delta t \frac{\partial \sum_i c_{i,\alpha} f_i^{col}/\rho}{\partial x_\alpha} - \frac{\Delta t^2}{2} \frac{\partial^2 \sum_i c_{i,\alpha} c_{i,\beta} f_i^{col}/\rho}{\partial x_\alpha \partial x_\beta} + \mathcal{O}(\Delta t^3)$$
$$= \Delta t \frac{\partial u_\alpha}{\partial x_\alpha} - \frac{\Delta t^2}{2} \frac{\partial^2 (p/\rho)}{\partial x_\alpha^2} - \frac{\Delta t^2}{2} \frac{\partial^2 u_\alpha u_\beta}{\partial x_\alpha \partial x_\beta} + \mathcal{O}(\Delta t^3)$$

where α and β are dummy index. It is clear that this operator gives a reasonable velocity divergence, together with a favorable numerical dissipation term to enhance the numerical stability as shown in term (I) in equation (21). In the end, the pressure field is updated following equation (2) as

$$p(t + \Delta t) = p(t) + \rho c^2 \sum_i \left(\left(\frac{f_i^{col}}{\rho} \right)^* - \frac{f_i^{col}}{\rho} \right)$$
$$= p(t) + \Delta t \rho c^2 \left[\frac{\partial u_\alpha}{\partial x_\alpha} - \underbrace{\frac{\Delta t}{2} \frac{\partial^2 (p/\rho)}{\partial x_\alpha^2} - \frac{\Delta t}{2} \frac{\partial^2 u_\alpha u_\beta}{\partial x_\alpha \partial x_\beta}}_{\text{I}} \right] + \mathcal{O}(\Delta t^3) \tag{21}$$

We here use c instead of the physical speed of sound c_{son} for the speed of the acoustic wave. They are related through:

$$c = \frac{c_{son}}{a} \tag{22}$$

with a a positive constant. This is useful to improve the stability of the scheme. This macroscopic reconstruction of the pressure field is a novelty, to the authors' knowledge.

C. A finite difference scheme for the Allen-Cahn equation

The macroscopic quantities p, ρ, u are all valid in both of the two phases that we will be studying, even at the interface. The fact that we don't track different variables for the two fluids make it inevitable that we have to add another field to track the interface. The order parameter takes continuous values between -1 and 1 and helps defining interfaces as isovalues $\phi = 0$. Note that it is more common to find order parameters ranging from 0 to 1 but this is strictly equivalent if we slightly modify the right-hand side (RHS) of (3).

One of the challenges of solving athermal multiphase flows is to correctly choose and discretize the phase-field equation. We would like to just advect the field ϕ with the flow velocity but this is no easy task due to steep numerical gradients which force the use of special numerical methods (such as a TVD (Total Variation Dimishing) scheme) and due to numerical diffusion which tends to widen the interface. The goal is then to design a sharpening method which is stable and don't alter too much the shape interface. One approach has been to use equations like equation (3) which is called an Allen-Cahn equation [64]. Right-hand side terms are composed of a diffusive and an anti-diffusive term which are there to control the width of the interface W over time. Note that different forms of this equation have been developed through the years. The chosen formulation has one advantage, it is simple and local. It also has some limitations, it is not conservative and can exhibits some non-physical behaviors, e.g. in presence of droplets of different sizes. These limitations can be lifted via more complex formulations, see for instance [38, 39].

The system (1 - 3) is typically studied in the phase-field framework. Good results have been recently published [33, 36, 37]. The vast majority of publications with this method use a double distribution function, which means that the equation evolving the order parameter is solved with a specific LBM scheme. However, in this work, we will follow the footsteps of Shao and Shu [65] and Wu et al. [66] and solve ϕ on the same mesh as the LBM scheme but with a finite-volume method. This framework is called hybrid LBM [67]. The idea is to have more flexibility in the discretization of this equation while keeping the advantages of a Lattice-Boltzmann scheme for the core of the fluid. It is then possible to use TVD schemes, which seems advisable knowing that we have to face steep gradients. In their paper, Shao and Shu use a third order TVD Runge-Kutta and a WENO5 to solve a Cahn-Hilliard equation [68]. They obtained impressive results at high density ratios. The second order of the LBM core being the limiting one there, we will investigate whether it is possible to get correct solutions even with a second order MUSCL scheme in space. The choice of the Allen-Cahn equation is partly due to the fact that it is simple, requiring only second order derivatives contrary to the Cahn-Hilliard equation which requires fourth order derivatives. Knowing that isotropy of derivatives is a major source of error [54], it seems wise to limit the order of them, especially when dealing with steep gradients.

In this work, the 2D MUSCL introduced by Yoo et al. [69] is adopted for the advection part (the LHS of (3)). This scheme has been proven to be second order even in diagonal directions, an important feature for the isotropy of our overall scheme. We use a minmod limiter [70] defined for a direction x by:

$$\Delta_x = \text{minmod}\left(\phi\left(x\right) - \phi\left(x - \Delta x\right), \phi\left(x + \Delta x\right) - \phi\left(x\right)\right) \tag{23}$$

$$\tag{24}$$

where

$$\text{minmod}\left(a, b\right) = \begin{cases} 0 & \text{if } a \times b < 0 \\ b & \text{else if } |b| < |a| \\ a & \text{else if } |a| < |b| \end{cases} \tag{25}$$

The discretization of the LHS of (3) is done via:

$$\frac{\phi\left(t + \Delta t\right) - \phi\left(t\right)}{\Delta t} + u_x \frac{\Delta F\left(\phi\left(t\right)\right)}{\Delta x} = 0 \tag{26}$$

We here describe the steps to get the flux along the x direction [48].

$$\begin{cases} \psi^R = \phi + \dfrac{1}{2}\Delta_x & (27) \\ \psi^L = \phi - \dfrac{1}{2}\Delta_x & (28) \end{cases}$$

$$\begin{cases} \overline{\psi^R} = \psi^R - \dfrac{u}{2}\Delta_x - \dfrac{v}{2}\Delta_y & (29) \\ \overline{\psi^L} = \psi^L - \dfrac{u}{2}\Delta_x - \dfrac{v}{2}\Delta_y & (30) \end{cases}$$

$$\begin{cases} \Delta F\left(\phi\right) = \overline{\psi^R}\left(x\right) - \overline{\psi^R}\left(x - \Delta x\right) & \text{if } u\left(x\right) + u\left(x + \Delta x\right) \geq 0 \quad (31) \\ \Delta F\left(\phi\right) = \overline{\psi^L}\left(x + \Delta x\right) - \overline{\psi^L}\left(x\right) & \text{otherwise} \quad (32) \end{cases}$$

For the RHS, we have many choices. We decide to discretize the gradients in an isotropic manner with the second order centered operator (16) while the Laplacian is discretized in the following way:

$$\frac{2}{c_s^2 \Delta t^2} \sum_i^N \omega_i \left[\phi\left(x + c_i \Delta t\right) - \phi\left(x\right)\right] = \Delta\phi + \mathcal{O}\left(\Delta x^2\right) \tag{33}$$

III. VALIDATIONS

Now that the numerical scheme of this study has been presented we will apply it to some academic test cases namely a Poiseuille flow with several phases, a Rayleigh-Taylor instability, and a Laplace test case and an oscillating droplet. This section concludes with a more complex case: liquid jet simulations in different regimes.

Test 1: Poiseuille (III A)**:** Validation of viscous shear stress

Test 2: Laplace (III B)**:** Validation of surface tension

Test 3: Oscillating droplet (III C)**:** Validation of surface tension with a moving droplet

Test 4: Rayleigh-Taylor instability (III D)**:** 2D validation of gravity and shear-induced effects

Test 5: Jets (III E)**:** Validation of breakup regimes

For these numerical studies, we will set to $M = \overline{\tau} c_s^2$. $\overline{\tau}$ is the relaxation time of the LBM solver defined in (11).

A. Poiseuille

The Poiseuille flow is one of the few test cases for which we have a theoretical solution, even with several phases. We study here a two-phase three-layer flow defined by:

$$\phi\left(x,y\right) = \tanh\left(-\frac{|y|-a}{W}\right) \tag{34}$$

A lighter phase is present near the walls, while a denser phase lies in the center.

Non-slip conditions are applied on top and bottom walls $y = 0$ and $y = N_y$ and the simulation is periodic along the x direction. The theoretical solution is a combination of three parabolae:

$$u_x\left(z\right) = \begin{cases} A_1 z^2 + C_1 & (0 \leq |z| \leq a) \\ A_2 z^2 + B_2 z + C_2 & (a \leq |z| \leq b) \end{cases}$$

with $z = y - b$, $a = N_y/4$, $b = N_y/2$, and:

$$\begin{aligned} A_1 &= -\frac{G}{2\rho_1\nu_1}; \quad A_2 = -\frac{G}{2\rho_2\nu_2} \\ B_2 &= 2\left(A_1\gamma - A_2\right)a \\ C_1 &= \left(A_2 - A_1\right)a^2 - B_2\left(b - a\right) - A_2b^2 \\ C_2 &= -A_2b^2 - B_2b \end{aligned}$$

with G the imposed gravity, ρ_k the density of phase k, ν_k the viscosity of phase k, and γ the density ratio.

We present results in Figure 1 for density ratios $\gamma = 10$ and $\gamma = 1000$. The results match very well with expected values.

We also present a convergence study in Figure 2 on the case at density ratio 10 with meshes of 125, 250 and 500 and 1000 points. We can clearly see a second order convergence.

B. Laplace

The previous Poiseuille test case enables us to validate the viscous part of the scheme, the Laplace test case will show that we also correctly recover surface tension. The goal is to simulate a droplet of phase 1 in a quiescent atmosphere of phase 2. Surface tension should produce a drop of pressure between inside and outside the droplet according to the Young-Laplace law which states that:

$$\Delta p = \frac{\sigma}{R} \tag{35}$$

where Δp is the drop of pressure, σ is the surface tension coefficient and R is the radius of the droplet.

The parameters of the simulation are: $\Delta x = 10^{-2}$m, $W = 3\Delta x$, $\nu = 10^{-3}\mathrm{m/s}^{-1}$, and a speed of sound of 300 m/s. We chose a grid of 200×200 points. $W = 3\Delta x$ means 15 points in the interface because the form of ϕ is chosen as an hyperbolic tangent. The goal was to test different size of droplets (20, 30 and 40 points in the radius), different density ratios ($\gamma = 4$, 100, 1000) and different surface tension coefficients. In the end, this last parameter didn't influence much the computation and the following results are presented for $\sigma = 0.01\mathrm{kg/s}^2$. We present the results in Table I.

We found that the results are acceptable, the interesting fact being that the main factor influencing them is the size of the droplet and not the density ratio. We also

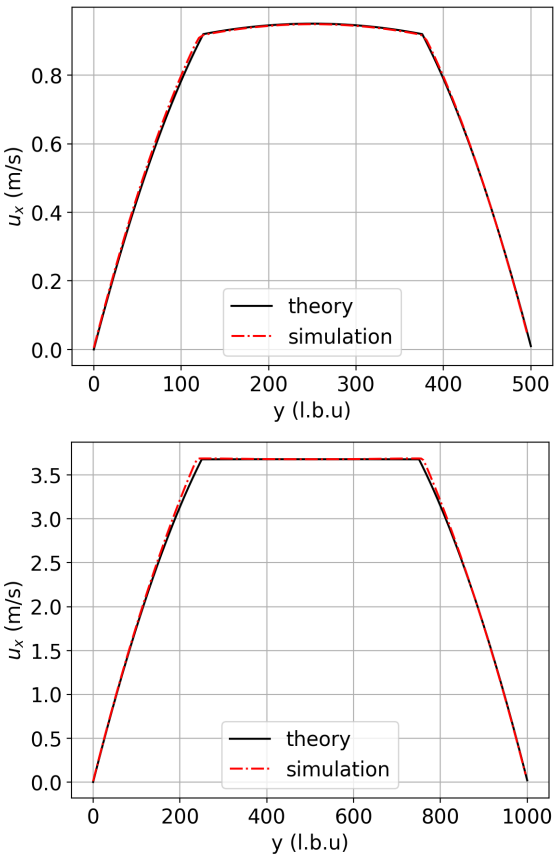

Figure 1: Poiseuille test case; Left: $\gamma = 10$ with 500 points; Right: $\gamma = 1000$ with 1000 points

present the pressure profiles in Figure 3 which show no sign of oscillation even at $\gamma = 1000$. On the left, the 2D profile is indeed circular whereas with schemes presenting anisotropy problems, the droplet quickly tends to become a square. On the right, we present a scatter plot of pressure as a function of the radius, showing an excellent level of isotropicity.

C. Oscillating Droplet

Another interesting test case related to surface tension is the oscillating droplet. The initial condition is composed of an ellipsoidal droplet which will tend to become spher-

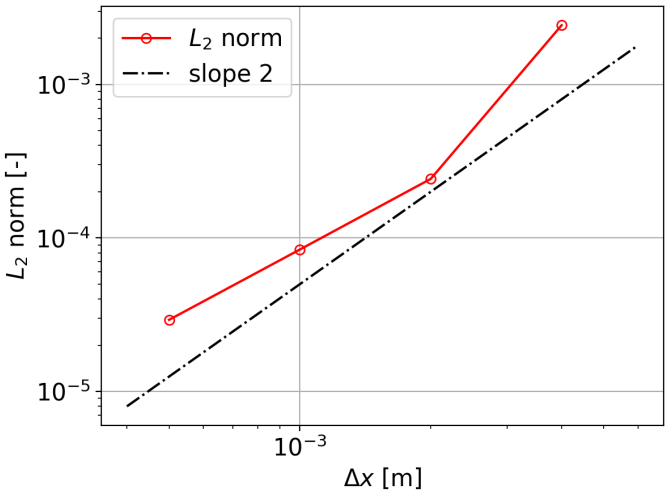

Figure 2: Convergence study for the case $\gamma = 10$

γ \ R	20	30	40
4	2.16%	0.93%	0.54%
100	2.31%	1.19%	0.77%
1000	2.52%	1.37%	1.07%

Table I: Errors for the Laplace test

ical after some oscillations. A theoretical solution for the period of these oscillations can be derived within the inviscid theory [71, 72]:

$$T_{\text{theorical}} = 2\pi\sqrt{\frac{(\rho_1 + \rho_2)\, r^3}{6\sigma}} \tag{36}$$

Note that this test case not only has to simulate the surface tension but also the movement of the droplet, both of which possibly leading to errors. The configuration is the following: $W = 4\Delta x$, the speed of sound is still 300m/s, we chose the viscosity as low as possible while being stable to compare to the inviscid theory, $\nu = 8 \times 10^{-7}\text{m}^2/\text{s}^{-1}$. The mesh is 300x300 points. The initial profile of ϕ is:

$$\phi(x, y) = -\tanh\frac{\sqrt{\frac{(x - x_0)^2}{a^2} + \frac{(y - y_0)^2}{b^2}} - R}{W} \tag{37}$$

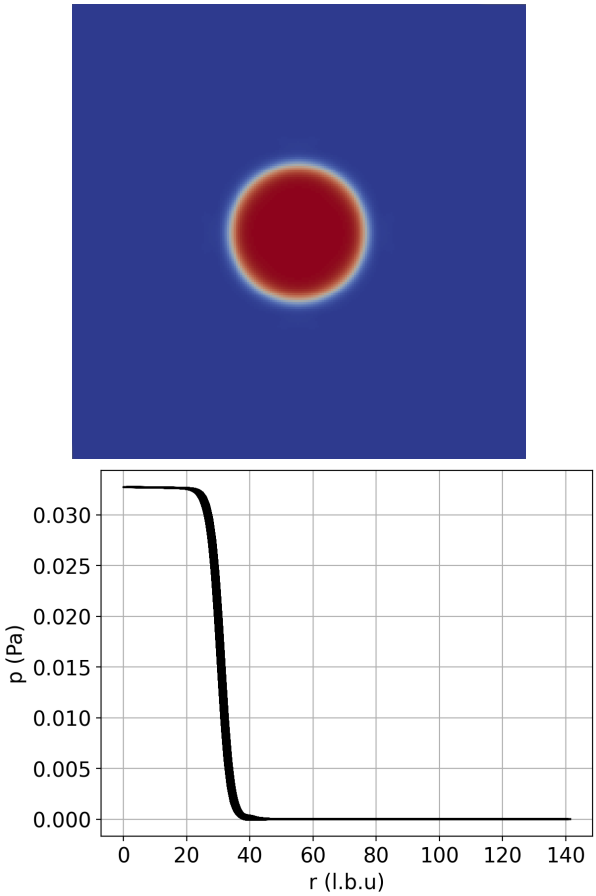

Figure 3: Left: pressure field, Right: pressure as a function of radial distance to the droplet's center ; $\gamma = 1000$ and $R = 30$

with (x_0, y_0) the center of the domain and $a = \sqrt{3/2}$, $b = 1/a$.

We compute the kinetic energy as a function of time (see Figure 4). A minimum value means that the droplet has an ellipsoidal shape (with zero velocity), a maximum value means that the droplet is spherical (maximum velocity). We then deduce that the period of oscillations of the kinetic energy is twice the period we are trying to measure (oscillations of the droplet). The last plot in Figure 4 presents the same three results but adimentionalized with the theoretical period of oscillations.

The three simulations have the same physical parameters except the density ratio γ. We can clearly see that the period of oscillation diminishes with this variable, which

means that low-density ratio simulations may be less precise because the oscillations are faster.

The model is stable even at higher ratios (eg 1000) but it becomes harder and harder to see the oscillations which are damped very quickly. The results are presented in Table II in the case where $\sigma = 0.1\text{kg/s}^2$. We again report the same level of errors with different values of σ.

γ	error
4	15.6 %
10	13.0 %
100	2.9 %

Table II: Errors on the period for the oscillating droplet test case

These results are of the same order of magnitude as what can be found in the literature [34]. It may seem unintuitive that the error decreases with the density ratio but we realized that the width of the interface was a major factor impacting the results. It seems that the resolution of the Allen-Cahn equation has important consequences on the results of the simulation. Indeed, different discretization and different W can lead to different shapes of the interface. Still this test case shows that the model correctly recovers the target surface tension although with undershoots of a few percents. It also shows that the code is stable for high density ratios with a moving interface.

D. Rayleigh-Taylor instability

The Rayleigh-Taylor instability is a phenomenon very well known and studied. Many solvers have simulated it which gives interesting points of comparison.

The test case consists of a dense fluid lying above another lighter fluid. The system is unstable due to the action of gravity and the heavier fluid will flow into the lighter one, taking at the same time a very special shape which are presented for different times in Figure 5.

The initialization is done with the following ϕ profile:

$$\phi(x, y, t = 0) = \tanh \frac{y - L_y/2 - 0.1L_x \cos(2\pi x/L_x)}{W} \tag{38}$$

This test case is characterized by two dimensionless numbers, the Reynolds number

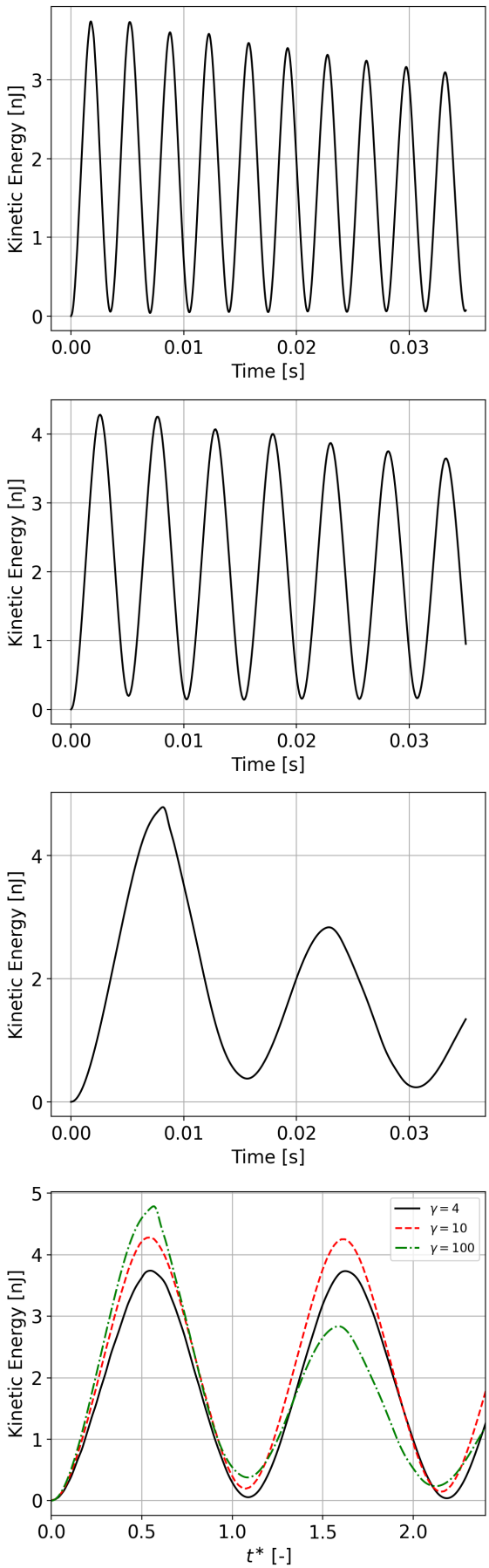

Figure 4: Oscillations of kinetic energy for density ratios 4, 10, and 100, for the same simulated physical time (0.035s); bottom right: same results adimentionalized with the theoretical period of oscillations

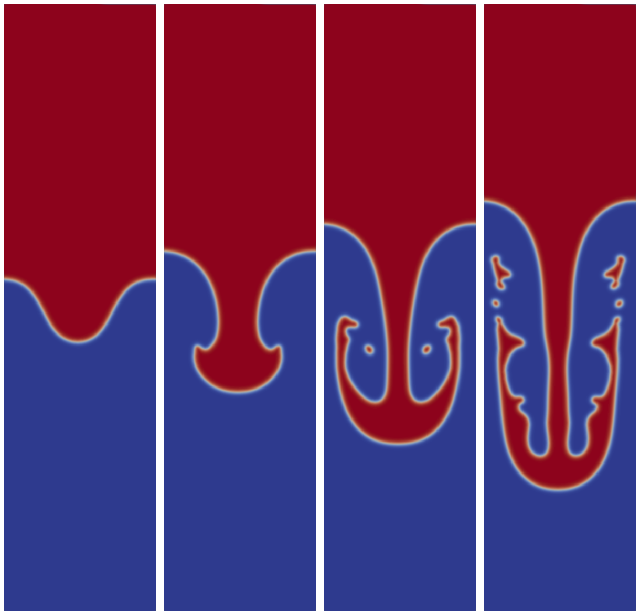

Figure 5: Rayleigh-Taylor instability for Re = 2048 and At = 0.5, at adimensionalized times $t^* = 1, 2, 3, 4$

and the Atwood number (representing the density ratio). They are defined by:

$$\mathrm{Re} = \frac{\sqrt{|g|}L_x^{3/2}}{\nu} \tag{39}$$

$$\mathrm{At} = \frac{\rho_1 - \rho_2}{\rho_1 + \rho_2} \tag{40}$$

with g the gravity; the velocity reference for the Reynolds being $U_0 = \sqrt{|g|\,L_x}$. We set here Re = 2048 and At = 0.5 (which corresponds to $\gamma = 3$).

We will compare the position and velocity of two points defined on the interface by $x = 0$ and $x = L_x/2$. We compare with the results of Reis [33] which have been validated against different solvers. We can see that the position of the interface match nearly exactly. However we have a little offset in one velocity after some time.

E. Jets

Lattice-Boltzmann multiphase solvers have been struggling with stability, especially when combining high density ratios with high Reynolds which is often the case in

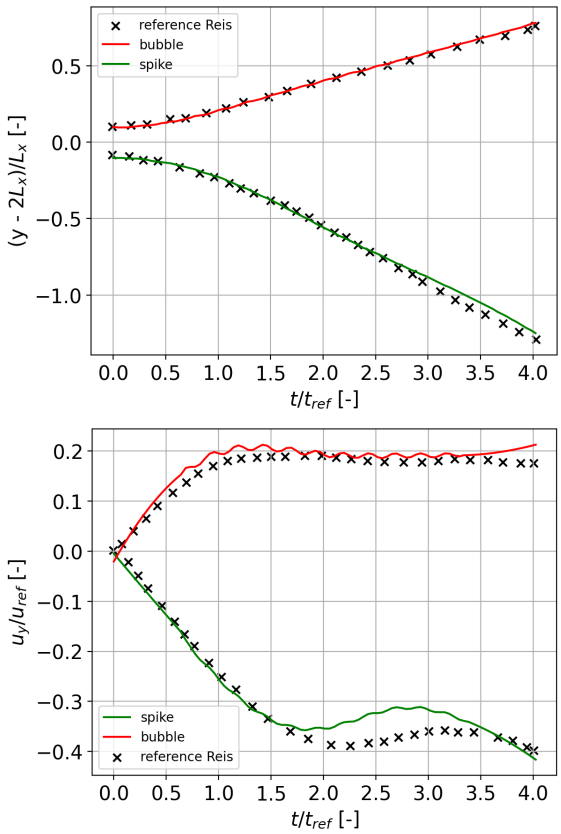

Figure 6: Interface position and velocity for when Re = 2048 and At = 0.5

industrial configurations. We present here several jet simulations to show the abilities of our solver on this topic.

We theoretically know the general behavior (regime) of a jet thanks to two adimensional numbers:

- Re $= DU/\nu$ the Reynolds number, which compares inertial and viscous forces, with D the diameter of the jet, U the jet velocity and ν its kinematic viscosity,
- Oh $= \mu/\sqrt{\rho\sigma D} = \mathrm{We}^{1/2}/\mathrm{Re}$ the Ohnesorge number, which compares the viscous and the capillary timescales.

with We $= \rho U^2 D/\sigma$ the Weber number, which compares the inertial and capillary forces.

The map in Figure 7 classifies three main breakup regimes [73] for a jet according

to its Ohnesorge and Reynolds numbers:

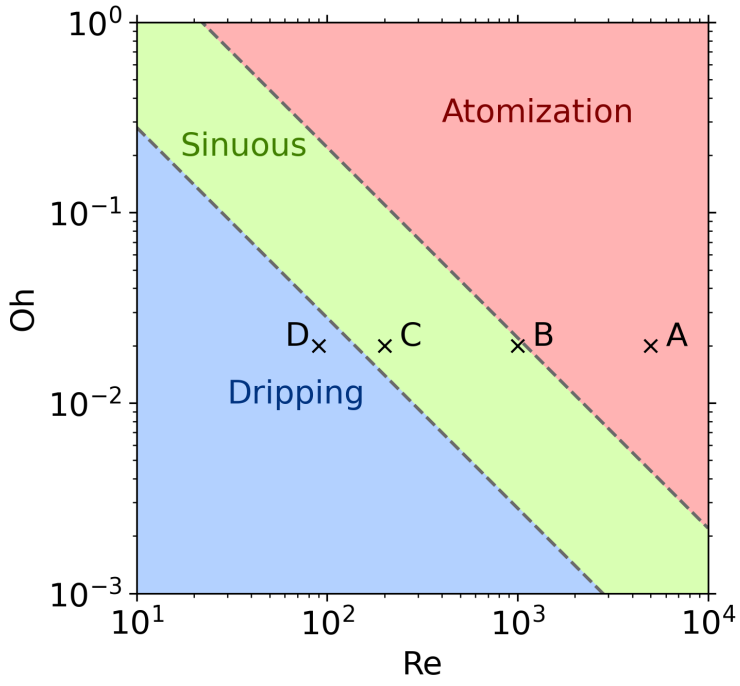

Figure 7: Map of jet breakup regimes as a function of Ohnesorge and Reynolds numbers

We will show through different simulations (A-C) that we can correctly recover the expected behaviors. We chose a constant Ohnesorge number of 0.02 and the diameter of the jet is set to $N_y/10$. We should have of jet clearly in the atomization region, one in the high sinuous region (nearly atomizing), one in the low sinuous region (nearly dripping). Results are presented in Figure 8 for a mesh 2400x1200 points and a density ratio of 2.

If we look at the snapshots presented in Figure 8 from bottom to top we can clearly see the different breakup regimes of the jet for a constant Oh = 0.02 and varying Reynolds number. In the dripping region we see a breakup of the jet due to surface tension forces which produces droplets whose diameter is of the same order of magnitude as the one of the jet.

The sinous jet at Reynolds 200 is mostly affected by surface tension that is reducing the diameter of the jet in some places. However the jet is not dripping because surface tension isn't strong enough to break the jet apart. Overall the diameter of the jet is

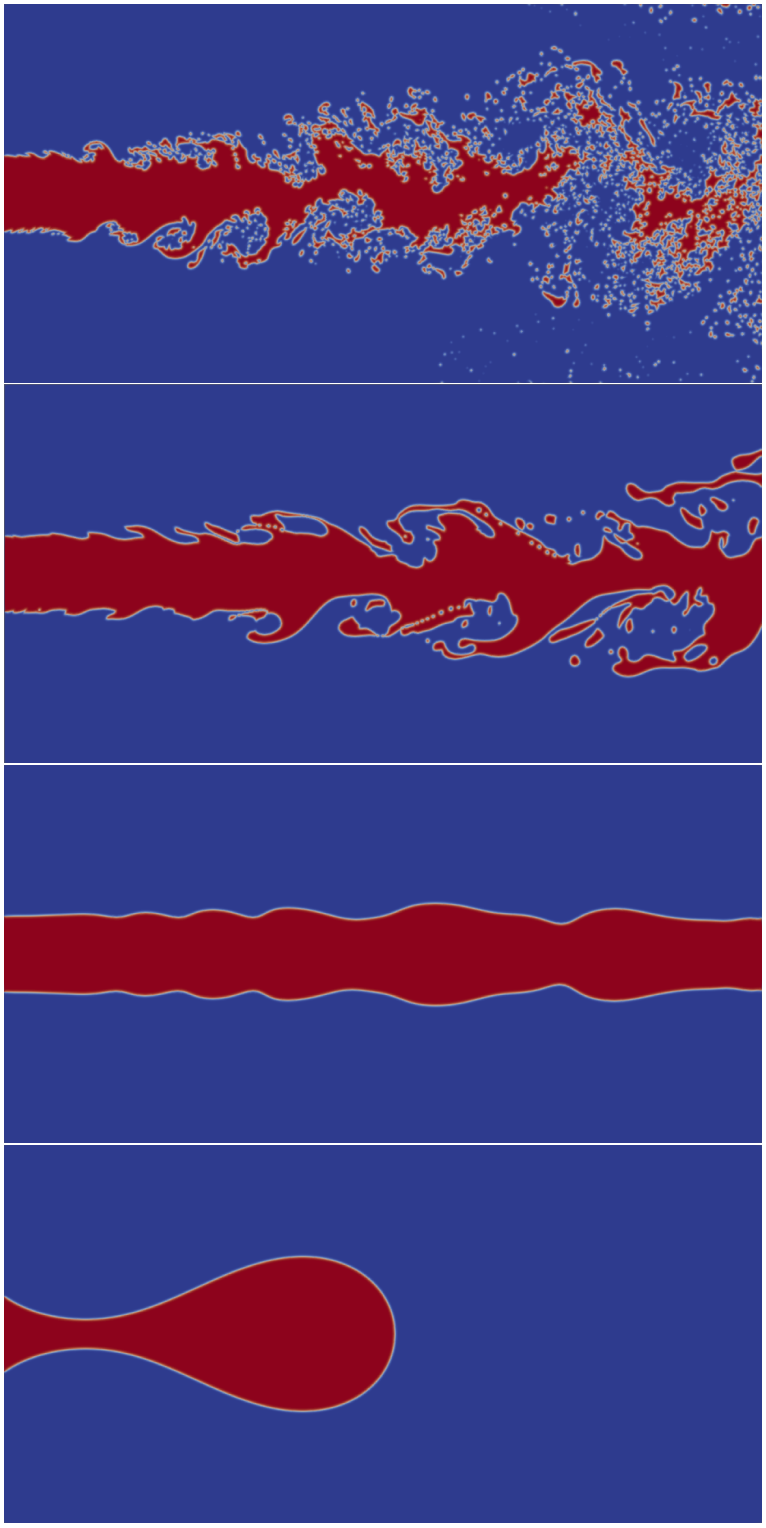

Figure 8: Jet simulations at $\gamma = 2$. Top (A): Atomization at Re = 5000; Middle (B): Sinuous flow at Re = 1000; Middle (C): Sinuous flow at Re = 200; Bottom (D): Dripping flow at Re = 90

not changing much. We don't observe any shear-induced instabilities.

We can clearly see a difference with the other sinuous jet, which is in fact near the atomization region while the first jet was near the dripping region. If the jet at Reynolds 1000 is mostly in one part we can see some small droplets detaching from the main dense phase region. The jet starts to impact a wider region at the outlet and we can notice some Kelvin-Helmholtz instabilities. Shear-induced instabilities seem to predominate over surface-tension forces.

Finally the jet is in the atomization region at Reynolds 5000. Lots of droplets are being created and the jet has the shape of a cone. Unfortunately atomization is creating a wide range of droplet sizes that we are not able to capture because the mesh is too coarse. We set the width of the interface to a certain value W so droplets with a radius less than this value cannot be captured. Another limiting factor is the size of the mesh for the same reasons. We have done this computation again with a 9600x4800 mesh (which is four times wider in all directions). Results are presented in Figure 9. The width of the interface is set to $W = 4$.

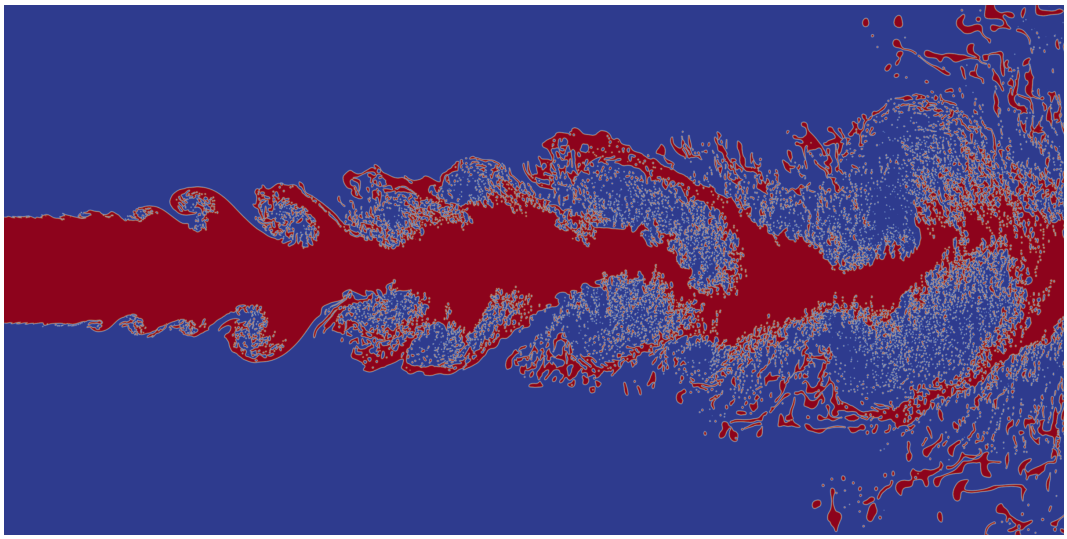

Figure 9: Jet at Reynolds 5000 and Ohnesorge 0.02 on a large 9600x4800 mesh

We can clearly see that way more droplets are being captured with this larger mesh. It is also easier to understand how atomization works on a basic level. Kelvin-Helmholtz vortices are created in an asymmetric fashion and grow in size along the x axis. They generate lots of small droplets and when they become "too" large, they break up.

IV. CONCLUSION

We have proposed new ideas in the phase-field framework in order to solve multiphase flows with a hybrid LBM / Finite Volume method. We designed a new equilibrium (13) leading to a new definition of the relaxation time τ (11) in order to circumvent the velocity discontinuity problems that we noticed. The resolution of an Allen-Cahn equation with a Finite Volume method is also a novelty to the author's knowledge. Note that recent articles have shown that improved ACE (see [38, 39]) could alleviate some inherent limitations of the original formulation. Combining these formulations with the present LBM model would be an interesting and necessary extension of the present work.

This scheme is also characterized by a recursive regularized collision kernel (A4), new correction terms computed from a Taylor expansion (17), the use of the low Mach number approximation, and a new macroscopic reconstruction for hydrodynamic pressure (21).

We tested the scheme against traditional academic test cases which proved that our method is stable even at high density ratio and high Reynolds and gives correct results when compared to the literature. The jet simulations prove that we can correctly recover the correct breakup regimes and the atomization phenomenon.

In the future we plan to bring more elements of the Level-Set method into our scheme to stabilize even more our computations and use a conservative Allen-Cahn equation. Moreover this work aims at being extended to thermal flows by changing the equation of state and adding an energy equation [48, 74].

V. ACKNOWLEDGMENTS

Centre de Calcul Intensif d'Aix-Marseille and GENCI (Grant 2023 - A0152B11951) are acknowledged for granting access to their high-performance computing resources. Part of this research was supported by the French project BALBUZARD funded by DGAC and supported by Next generation EU in the frame of "Plan national de Relance et de Résilience français (PNRR)" ; and by the ANR, Airbus, Fives-Pillard and SafranTech through the Industrial Chair Program LIBERTY ANR-23-CHIN-0005.

Appendix A: Recursive regularization

We define raw and Hermite moments of a distribution f respectively as:

$$\Pi^f_{\alpha_1 \dots \alpha_n} = \sum_{i=1}^{q} f_i \xi_{\alpha_1,i} \dots \xi_{\alpha_n,i} \tag{A1}$$

$$\mathcal{A}^f_{\alpha_1 \dots \alpha_n} = \sum_{i=1}^{q} f_i \mathcal{H}_{\alpha_1 \dots \alpha_n,i} \tag{A2}$$

with $\xi_{\alpha,i}$ the lattice velocities, $\mathcal{H}_{\alpha_1 \dots \alpha_n,i}$ Hermite polynomials of order n taken in ξ_i and q the number of lattices.

The non-equilibrium part of the distribution function f^{neq} is defined by:

$$f^{neq}_i = \omega_i \left(\mathcal{A}^{neq}_{\alpha\beta} \frac{\mathcal{H}_{\alpha\beta}}{2c_s^4} + \mathcal{A}^{neq}_{\alpha\beta\gamma} \frac{\mathcal{H}_{\alpha\beta\gamma}}{6c_s^6} \right) \tag{A3}$$

The second order Hermite moment $\mathcal{A}^{neq}_{\alpha\beta}$ can be calculated via the definition (A2) with $f^{neq} = f - f^{eq}$.

The third order Hermite moment is reconstructed recursively:

$$\begin{aligned} \mathcal{A}^{neq}_{xxy} &= u_y \mathcal{A}^{neq}_{xx} + 2u_x \mathcal{A}^{neq}_{xy} \\ \mathcal{A}^{neq}_{yyx} &= u_x \mathcal{A}^{neq}_{yy} + 2u_y \mathcal{A}^{neq}_{xy} \end{aligned} \tag{A4}$$

These formulae are dependent on the lattice and are here presented only for D2Q9. See Malaspinas et al. [58] and Coreixas et al. [59] for further information.

It was found that such regularizations are pretty simple and have very good stability properties.

Appendix B: Chapman-Enskog analysis

Chapman-Enskog and Taylor expansions are really important for Lattice-Boltzmann schemes because they can be used to understand to which macroscopic continuous equations is consistent our scheme. Moreover, lattices that are often used in practice (D2Q9, D3Q19, D3Q27) don't have a lot of discrete velocities and introduce errors that can be quantified by these expansions [75]. We start from the value of $\Pi^{neq}_{\alpha\beta}$ obtained through a Taylor expansion by Farag et al. [76]. This term is linked to the stress tensor $\mathcal{T}_{\alpha\beta}$ and we will see that it needs to be corrected.

$$-\frac{1}{\tau}\Pi^{neq}_{\alpha\beta} = \frac{\partial \Pi_{\alpha\beta}}{\partial t} + \frac{\partial\left(\Pi_{\alpha\beta\gamma} - D^{eq}_{\alpha\beta\gamma}\right)}{\partial x_\gamma} - \Pi^{\mathcal{F}}_{\alpha\beta} + \mathcal{O}\left(\tau^2\right) \tag{B1}$$

As we don't know the non-equilibrium part of the third order moments, we cannot use (B1) straight away. We will neglect these terms in what is now equivalent to a Chapman-Enskog expansion:

$$-\frac{1}{\tau}\Pi^{neq}_{\alpha\beta} \simeq \frac{\partial \Pi^{eq}_{\alpha\beta}}{\partial t} + \frac{\partial\left(\Pi^{eq}_{\alpha\beta\gamma} - D^{eq}_{\alpha\beta\gamma}\right)}{\partial x_\gamma} - \Pi^{\mathcal{F}}_{\alpha\beta} + \mathcal{O}\left(\tau^2\right) \tag{B2}$$

We will use the equal sign in what follows.

Here, $\Pi^{\mathcal{F}}_{\alpha\beta}$ is the second order moment of some correction terms. We will show that this term is nonzero.

Let's assume that we have from the Navier-Stokes equations:

$$\frac{\partial \rho u_\alpha u_\beta}{\partial t} = -\frac{\partial \rho u_\alpha u_\beta u_\gamma}{\partial x_\gamma} - \frac{\partial\left(p\delta_{\alpha\gamma} - \mathcal{T}_{\alpha\gamma}\right)}{\partial x_\gamma} u_\beta - \frac{\partial\left(p\delta_{\beta\gamma} - \mathcal{T}_{\beta\gamma}\right)}{\partial x_\gamma} u_\alpha + \rho\mathcal{F}_\alpha u_\beta + \rho\mathcal{F}_\beta u_\alpha \tag{B3}$$

Here $\mathcal{F}_\alpha$ are some external forcing terms. We will be neglecting the derivatives of $\mathcal{T}_{\alpha\beta}$ in what follows.

Relation (B3) is useful because :

$$\frac{\partial \Pi^{eq}_{\alpha\beta}}{\partial t} = \frac{\partial \rho u_\alpha u_\beta}{\partial t} + \frac{\partial p\delta_{\alpha\beta}}{\partial t} \tag{B4}$$

Taking the divergence of $\Pi^{eq}_{\alpha\beta\gamma}$ leads to :

$$\frac{\partial \Pi^{eq}_{\alpha\beta\gamma}}{\partial x_\gamma} = \frac{\partial \rho u_\alpha u_\beta u_\gamma}{\partial x_\gamma} + \rho_0 c_s^2 \left(\frac{\partial u_\alpha}{\partial x_\beta} + \frac{\partial u_\beta}{\partial x_\alpha} + \frac{\partial u_\gamma}{\partial x_\gamma}\delta_{\alpha\beta}\right) \tag{B5}$$

We have :

$$-\frac{1}{\tau}\Pi^{neq}_{\alpha\beta} = \rho_0 c_s^2 \left(\frac{\partial u_\alpha}{\partial x_\beta} + \frac{\partial u_\beta}{\partial x_\alpha} - \frac{2}{D}\frac{\partial u_\gamma}{\partial x_\gamma}\delta_{\alpha\beta}\right) \tag{B6}$$

$$+ \frac{\partial p}{\partial t}\delta_{\alpha\beta} + \rho_0 c_s^2 \left(1 + \frac{2}{D}\right)\frac{\partial u_\gamma}{\partial x_\gamma}\delta_{\alpha\beta} \tag{B7}$$

$$- \frac{\partial p}{\partial x_\alpha}u_\beta - \frac{\partial p}{\partial x_\beta}u_\alpha \tag{B8}$$

$$+ \rho\mathcal{F}_\alpha u_\beta + \rho\mathcal{F}_\beta u_\alpha - \frac{\partial D^{eq}_{\alpha\beta\gamma}}{\partial x_\gamma} - \Pi^{\mathcal{F}}_{\alpha\beta} \tag{B9}$$

This analysis tells us that we would have $-\Pi^{neq}_{\alpha\beta} = \mathcal{T}_{\alpha\beta}$ only if $\tau\rho_0 c_s^2 = \mu$ which we asserted in equation (11) and if all the terms in (B7) - (B9) are null. This is not the case, which is why we need to impose some correction terms. It is clear that we can substract all the unwanted terms from the forcing term $\Pi^{\mathcal{F}}_{\alpha\beta}$.

First, let us give explicitly the formula of the isotropy defect $\mathcal{D}^{eq}_{\alpha\beta\gamma}$. It should compensate the terms xxx and yyy that are not correctly recovered in $\Pi^{eq}_{\alpha\beta\gamma}$. We have $\mathcal{A}^{eq}_{xxx} = \mathcal{A}^{eq}_{yyy} = 0$ because we can't impose them in D2Q9, so:

$$\mathcal{A}^{eq}_{xxx} = 0 \Rightarrow \Pi^{eq}_{xxx} = 3\rho c_s^2 u_x \tag{B10}$$

$$\mathcal{A}^{eq}_{yyy} = 0 \Rightarrow \Pi^{eq}_{yyy} = 3\rho c_s^2 u_y \tag{B11}$$

Our target moments are:

$$\Pi^{\text{target}}_{xxx} = \rho u_x^3 + 3\rho_0 c_s^2 u_x \tag{B12}$$

$$\Pi^{\text{target}}_{yyy} = \rho u_y^3 + 3\rho_0 c_s^2 u_y \tag{B13}$$

So we have:

$$D^{eq}_{xxx} = \Pi^{\text{target}}_{xxx} - \Pi^{eq}_{xxx} = \rho u_x^3 + 3\left(\rho_0 - \rho\right)c_s^2 u_x \tag{B14}$$

$$D^{eq}_{yyy} = \Pi^{\text{target}}_{yyy} - \Pi^{eq}_{yyy} = \rho u_y^3 + 3\left(\rho_0 - \rho\right)c_s^2 u_y \tag{B15}$$

Then:

$$\frac{\partial D^{eq}_{\alpha\beta\gamma}}{\partial x_\gamma} = \frac{\partial\left(\rho u_x^3 + 3\left(\rho_0 - \rho\right)c_s^2 u_x\right)}{\partial x}\mathcal{I}_{xx} + \frac{\partial\left(\rho u_y^3 + 3\left(\rho_0 - \rho\right)c_s^2 u_y\right)}{\partial y}\mathcal{I}_{yy} \tag{B16}$$

Finally the second order moment of the correction terms that we find is:

$$\Pi^{\mathcal{F}}_{\alpha\beta} = \rho\mathcal{F}_\alpha u_\beta + \rho\mathcal{F}_\beta u_\alpha + \frac{\partial p}{\partial t}\delta_{\alpha\beta} + \rho_0 c_s^2 \left(1 + \frac{2}{D}\right) \frac{\partial u_\gamma}{\partial x_\gamma}\delta_{\alpha\beta} - \frac{\partial p}{\partial x_\alpha}u_\beta - \frac{\partial p}{\partial x_\beta}u_\alpha - \frac{\partial D^{eq}_{\alpha\beta\gamma}}{\partial x_\gamma} \tag{B17}$$

---

[1] R. Saurel, P. Boivin, and O. Le Métayer, A general formulation for cavitating, boiling and evaporating flows, Computers and Fluids **128**, 53 (2016).

[2] B. Péden, J. Carmona, P. Boivin, T. Schmitt, B. Cuenot, and N. Odier, Numerical assessment of Diffuse-Interface method for air-assisted liquid sheet simulation, Computers and Fluids **266**, 106022 (2023).

[3] D. Nayigizente, *Unsteady simulations of liquid/gas interfaces in real gas flows using the Second Gradient theory*, Theses, Université Paris-Saclay (2021).

[4] S. Osher and J. A. Sethian, Fronts propagating with curvature-dependent speed: Algorithms based on hamilton-jacobi formulations, Journal of computational physics **79**, 12 (1988).

[5] F. Gibou, R. Fedkiw, and S. Osher, A review of level-set methods and some recent applications, Journal of Computational Physics **353**, 82 (2018).

[6] W. F. Noh and P. Woodward, Slic (simple line interface calculation), in *Proceedings of the fifth international conference on numerical methods in fluid dynamics June 28–July 2, 1976 Twente University, Enschede* (Springer, 2005) pp. 330–340.

[7] C. W. Hirt and B. D. Nichols, Volume of fluid (vof) method for the dynamics of free boundaries, Journal of computational physics **39**, 201 (1981).

[8] J. Carmona, *Modélisation des phénomènes diphasiques dans des injecteurs aéronautiques de type Airblast*, Theses, Institut National Polytechnique de Toulouse - INPT (2021).

[9] D. Fuster, G. Agbaglah, C. Josserand, S. Popinet, and S. Zaleski, Numerical simulation of droplets, bubbles and waves: state of the art, Fluid dynamics research **41**, 065001 (2009).

[10] L. Deike, W. K. Melville, and S. Popinet, Air entrainment and bubble statistics in breaking waves, Journal of Fluid Mechanics **801**, 91 (2016).

[11] O. Desjardins, V. Moureau, and H. Pitsch, An accurate conservative level set/ghost fluid method for simulating turbulent atomization, Journal of computational physics **227**, 8395 (2008).

[12] O. Desjardins, J. McCaslin, M. Owkes, and P. Brady, Direct numerical and large-eddy simulation of primary atomization in complex geometries, Atomization and Sprays **23** (2013).

[13] T. Krüger, H. Kusumaatmaja, A. Kuzmin, O. Shardt, G. Silva, and E. M. Viggen, *The lattice Boltzmann method*, Vol. 10 (Springer, 2017) pp. 4–15.

[14] A. Suss, I. Mary, T. Le Garrec, and S. Marié, Comprehensive comparison between the

lattice Boltzmann and Navier–Stokes methods for aerodynamic and aeroacoustic applications, Computers and Fluids **257**, 105881 (2023).

[15] B. Ljubomir, Quantum algorithm for the navier–stokes equations by using the streamfunction-vorticity formulation and the lattice boltzmann method, International Journal of Quantum Information **20**, 2150039 (2022).

[16] N. Fonio, P. Sagaut, and G. Di Molfetta, A fully quantum algorithm for hydrodynamic lattice gas cellular automata, arXiv preprint arXiv:2310.07362 (2023).

[17] J. A. R. Barraza and R. Deiterding, Towards a generalised lattice boltzmann method for aerodynamic simulations, Journal of Computational Science **45**, 101182 (2020).

[18] T. Coratger, G. Farag, S. Zhao, P. Boivin, and P. Sagaut, Large-eddy lattice-Boltzmann modeling of transonic flows, Physics of Fluids **33**, 10.1063/5.0064944 (2021).

[19] H. Maeyama, T. Imamura, J. Osaka, and N. Kurimoto, Unsteady aerodynamic simulations by the lattice boltzmann method with near-wall modeling on hierarchical cartesian grids, Computers & Fluids **233**, 105249 (2022).

[20] K. Kusano, K. Yamada, and M. Furukawa, Aeroacoustic simulation of broadband sound generated from low-mach-number flows using a lattice boltzmann method, Journal of Sound and Vibration **467**, 115044 (2020).

[21] T. Astoul, G. Wissocq, J. F. Boussuge, A. Sengissen, and P. Sagaut, Lattice Boltzmann method for computational aeroacoustics on non-uniform meshes: A direct grid coupling approach, Journal of Computational Physics **447**, 110667 (2021), arXiv:2004.14887.

[22] M. Safdari Shadloo, Numerical simulation of compressible flows by lattice boltzmann method, Numerical Heat Transfer, Part A: Applications **75**, 167 (2019).

[23] C. Coreixas and J. Latt, Compressible lattice Boltzmann methods with adaptive velocity stencils: An interpolation-free formulation, Physics of Fluids **32**, 1 (2020), arXiv:2009.13426.

[24] G. Farag, T. Coratger, G. Wissocq, S. Zhao, P. Boivin, and P. Sagaut, A unified hybrid lattice-Boltzmann method for compressible flows: Bridging between pressure-based and density-based methods, Physics of Fluids **33**, 1 (2021).

[25] S. A. Hosseini, *Development of a lattice Boltzmann-based numerical method for the simulation of reacting flows*, Theses, Université Paris-Saclay ; Otto-von-Guericke-Universität Magdeburg (2020).

[26] G. Wissocq, S. Taileb, S. Zhao, and P. Boivin, A hybrid lattice Boltzmann method for gaseous detonations, Journal of Computational Physics **494**, 112525 (2023).

[27] H. Huang, M. Sukop, and X.-Y. Lu, *Multiphase Lattice Boltzmann Methods* (Wiley-Blackwell, 2015).

[28] D. H. Rothman and J. M. Keller, Immiscible cellular-automaton fluids, Journal of Statistical Physics **52**, 1119 (1988).

[29] S. Leclaire, N. Pellerin, M. Reggio, and J. Y. Trépanier, A multiphase lattice Boltzmann method for simulating immiscible liquid-liquid interface dynamics, Applied Mathematical Modelling **40**, 6376 (2016).

[30] G. Wang, U. D'ortona, and P. Guichardon, Improved partially saturated method

for the lattice boltzmann pseudopotential multicomponent flows, Physical Review E 10.1103/PhysRevE.107.035301ï (2023).

[31] T. Mitchell, Development of a multiphase lattice Boltzmann model for high-density and viscosity ratio flows in unconventional gas wells, Phd (2019).

[32] T. Inamuro, T. Ogata, S. Tajima, and N. Konishi, A lattice Boltzmann method for incompressible two-phase flows with large density differences, Journal of Computational Physics **198**, 628 (2004).

[33] T. Reis, A lattice Boltzmann formulation of the one-fluid model for multiphase flow, Journal of Computational Physics **453**, 110962 (2022).

[34] T. Lafarge, P. Boivin, N. Odier, and B. Cuenot, Improved color-gradient method for lattice Boltzmann modeling of two-phase flows, Physics of Fluids **33**, 10.1063/5.0061638 (2021).

[35] H. Wang, X. Yuan, H. Liang, Z. Chai, and B. Shi, A brief review of the phase-field-based lattice boltzmann method for multiphase flows, Capillarity **2**, 33 (2019).

[36] W. Li, D. Liu, M. Desbrun, J. Huang, and X. Liu, Kinetic-Based Multiphase Flow Simulation, IEEE Transactions on Visualization and Computer Graphics **27**, 3318 (2021).

[37] W. Li, Y. Ma, X. Liu, and M. Desbrun, Efficient kinetic simulation of two-phase flows, ACM Transactions on Graphics **41**, 1 (2022).

[38] X. Liu, Z. Chai, and B. Shi, Improved hybrid allen-cahn phase-field-based lattice boltzmann method for incompressible two-phase flows, Physical Review E **107**, 035308 (2023).

[39] Y. Hu, D. Li, L. Jin, X. Niu, and S. Shu, Hybrid allen-cahn-based lattice boltzmann model for incompressible two-phase flows: The reduction of numerical dispersion, Physical Review E **99**, 023302 (2019).

[40] A. J. Chorin, A numerical method for solving incompressible viscous flow problems, Journal of Computational Physics **2**, 12 (1967).

[41] J. R. Clausen, Entropically damped form of artificial compressibility for explicit simulation of incompressible flow, Physical Review E - Statistical, Nonlinear, and Soft Matter Physics **87**, 1 (2013).

[42] A. Toutant, Numerical simulations of unsteady viscous incompressible flows using general pressure equation, Journal of Computational Physics **374**, 822 (2018), arXiv:2005.06448.

[43] D.J. Korteweg, Sur la forme que prennent les équations du mouvement des fluides si l'on tient compte des forces capillaires causées par des variations de densité considérables mais continues, Archives Néerlandaises des Sciences exactes et naturelles (1901).

[44] S. Popinet, Numerical Models of Surface Tension, Annual Review of Fluid Mechanics **50**, 49 (2018).

[45] R. Saurel and C. Pantano, Diffuse-interface capturing methods for compressible two-phase flows, Annual Review of Fluid Mechanics **50**, 105 (2018).

[46] M. Pelletier, *Diffuse interface models and adapted numerical schemes for the simulation of subcritical to supercritical flows*, Theses, Université Paris Saclay (COmUE) (2019).

[47] A. K. Kapila, R. Menikoff, J. B. Bdzil, S. F. Son, and D. S. Stewart, Two-phase modeling of deflagration-to-detonation transition in granular materials: Reduced equations,

Physics of Fluids **13**, 3002 (2001).

[48] G. Farag, S. Zhao, T. Coratger, P. Boivin, G. Chiavassa, and P. Sagaut, A pressure-based regularized lattice-Boltzmann method for the simulation of compressible flows, Physics of Fluids **32**, 10.1063/5.0011839 (2020).

[49] Z. Guo, C. Zheng, and B. Shi, Discrete lattice effects on the forcing term in the lattice Boltzmann method, Physical Review E - Statistical Physics, Plasmas, Fluids, and Related Interdisciplinary Topics **65**, 6 (2002).

[50] H. Huang, J. J. Huang, X. Y. Lu, and M. C. Sukop, On simulations of high-density ratio flows using color-gradient multiphase lattice boltzmann models, International Journal of Modern Physics C **24**, 1 (2013).

[51] Z. X. Wen, Q. Li, Y. Yu, and K. H. Luo, Improved three-dimensional color-gradient lattice Boltzmann model for immiscible two-phase flows, Physical Review E **100**, 10.1103/PhysRevE.100.023301 (2019), arXiv:1904.03618.

[52] F. Renard, *Hybrid Lattice Boltzmann Method for Compressible Flows*, Ph.D. thesis, Aix-Marseille Université (2021).

[53] M. Taha, S. Zhao, A. Lamorlette, J.-l. Consalvi, and P. Boivin, International Journal of Thermal Sciences Large eddy simulation of fire-induced flows using Lattice-Boltzmann methods, International Journal of Thermal Sciences **197**, 108801 (2024).

[54] S. Leclaire, M. Reggio, and J. Y. Trépanier, Isotropic color gradient for simulating very high-density ratios with a two-phase flow lattice Boltzmann model, Computers and Fluids **48**, 98 (2011).

[55] P. Mora, G. Morra, and D. A. Yuen, Optimal surface-tension isotropy in the Rothman-Keller color-gradient lattice Boltzmann method for multiphase flow, Physical Review E **103**, 1 (2021).

[56] T. Lafarge, *Investigation of Lattice Boltzmann methods applied to multiphase flows*, Theses, Institut National Polytechnique de Toulouse - INPT (2022).

[57] A. De Rosis and E. Enan, A three-dimensional phase-field lattice Boltzmann method for incompressible two-components flows, Physics of Fluids **33**, 10.1063/5.0046875 (2021).

[58] O. Malaspinas, Increasing stability and accuracy of the lattice Boltzmann scheme: recursivity and regularization, arXiv , 1 (2015), arXiv:1505.06900.

[59] C. Coreixas, G. Wissocq, G. Puigt, J.-F. F. Boussuge, and P. Sagaut, Recursive regularization step for high-order lattice Boltzmann methods, Physical Review E **96**, 1 (2017), arXiv:1704.04413.

[60] J. Jacob, O. Malaspinas, and P. Sagaut, A new hybrid recursive regularised bhatnagar–gross–krook collision model for lattice boltzmann method-based large eddy simulation, Journal of Turbulence **19**, 1051 (2019).

[61] C. G. Coreixas, *High-order extension of the recursive regularized lattice Boltzmann method*, Theses, Institut National Polytechnique de Toulouse - INPT (2018).

[62] G. Wissocq, Investigation of lattice Boltzmann methods for turbomachinery secondary air system simulations, PhD thesis (2019).

[63] P. Bhatnagar, E. Gross, and M. Krook, A Model for Collision Proceses in Gases. I. Small

Amplitude Processes in Charged and Neutral One-Component Systems, Physical Review 10.1103/physrev94.511 (1953).

[64] S. M. Allen and J. W. Cahn, Mechanisms of phase transformations within the miscibility gap of Fe-rich Fe-Al alloys, Acta Metallurgica **24**, 425 (1976).

[65] J. Y. Shao and C. Shu, A hybrid phase field multiple relaxation time lattice Boltzmann method for the incompressible multiphase flow with large density contrast, International Journal for Numerical Methods in Fluids **77**, 526 (2015).

[66] J. Wu, C. Liu, and N. Zhao, Dynamics of falling droplets impact on a liquid film: Hybrid lattice Boltzmann simulation, Colloids and Surfaces A: Physicochemical and Engineering Aspects **472**, 92 (2015).

[67] Y. Feng, P. Boivin, J. Jacob, and P. Sagaut, Hybrid recursive regularized thermal lattice Boltzmann model for high subsonic compressible flows, Journal of Computational Physics **394**, 82 (2019).

[68] J. W. Cahn and J. E. Hilliard, Free energy of a nonuniform system. I. Interfacial free energy, The Journal of Chemical Physics **28**, 258 (1958).

[69] H. Yoo, G. Wissocq, J. Jacob, J. Favier, and P. Sagaut, Compressible lattice Boltzmann method for rotating overset grids, Phys. Rev. E **107**, 045306 (2023).

[70] B. van Leer, Upwind and High-Resolution Methods for Compressible flow, 16th AIAA Computational Fluid Dynamics Conference **3** (2003).

[71] L. Rayleigh, On the instability of jets, Proceedings of the London Mathematical Society **s1-10**, 4 (1878), https://londmathsoc.onlinelibrary.wiley.com/doi/pdf/10.1112/plms/s1-10.1.4.

[72] D. Fyfe, E. Oran, and M. Fritts, Surface tension and viscosity with lagrangian hydrodynamics on a triangular mesh, Journal of Computational Physics **76**, 349 (1988).

[73] S. Saito, A. De Rosis, A. Festuccia, A. Kaneko, Y. Abe, and K. Koyama, Color-gradient lattice Boltzmann model with nonorthogonal central moments: Hydrodynamic melt-jet breakup simulations, Physical Review E **98**, 10.1103/PhysRevE.98.013305 (2018), arXiv:1804.08923.

[74] G. Wissocq, T. Coratger, G. Farag, S. Zhao, P. Boivin, and P. Sagaut, Restoring the conservativity of characteristic-based segregated models: Application to the hybrid lattice Boltzmann method, Physics of Fluids **34**, 046102 (2022).

[75] F. Renard, Y. Feng, J. F. o. Boussuge, and P. Sagaut, Improved compressible hybrid lattice Boltzmann method on standard lattice for subsonic and supersonic flows, Computers and Fluids **219**, 10.1016/j.compfluid.2021.104867 (2021), arXiv:2002.03644.

[76] G. Farag, S. Zhao, G. Chiavassa, and P. Boivin, Consistency study of Lattice-Boltzmann schemes macroscopic limit, Physics of Fluids **33**, 10.1063/5.0039490 (2021).